500 GHz–750 GHz Rectangular-Waveguide Vector-Network-Analyzer Calibrations

Dylan F. Williams, *Fellow, IEEE*

***Abstract*—We develop an uncertainty analysis that captures the dominant sources of measurement error in state-of-the-art WM-380 (WR 1.5) rectangular-waveguide vector-network-analyzer measurements over the frequency range 500–750 GHz. We use the analysis to assess thru-reflect-line, thru-short-match, and thru-short-radiating-open calibrations. The comparison shows that thru-short-match and thru-short-radiating-open calibrations outperform thru-reflect-line calibrations, and that this is true even when multiple lines and optimal averaging are used to improve the thru-reflect-line calibrations.**

***Index Terms*—Calibration, submillimeter wave, uncertainty analysis, vector network analyzer.**

I. Introduction

We investigate 500 GHz–750 GHz rectangular-waveguide vector-network-analyzer (VNA) calibrations. We identify the principal error contributions, compare calibration approaches, and develop a complete error analysis capable of estimating uncertainties due to variations in aperture sizes, burrs, corner rounding, and other errors, as well as E-plane, H-plane, and angular displacements, which, due to their quadratic nature, are not amenable to standard (linear) uncertainty analyses.

Bannister *et al.* developed one of the more complete and well-documented uncertainty analyses for rectangular waveguide in [1]. Reference [1] includes a useful set of tables for estimating the uncertainty of rectangular-waveguide calibrations from dimensional uncertainties. Kerr *et al.* presented a complementary analysis of rectangular waveguide discontinuities in [2], [3]. However, the impact of these flange discontinuities on VNA calibrations was not discussed. The European Association of National Metrology Institutes also has published a guideline for assessing VNA calibration uncertainty [4]. While the approach described in the guide requires access to precision transmission lines that are not generally available at submillimeter wavelengths, it is applicable to a large number of waveguides, including rectangular waveguide.

In this paper, we develop and verify analytic models for the dominant error mechanisms of rectangular-waveguide VNA measurements over the frequency range of 500–750 GHz. We first investigate analytic expressions for rectangular-waveguide discontinuities developed in [1], [5]–[9], comparing them to numerical simulations performed with Ansoft's High-Frequency Structure Simulator[1] (HFSS). This analysis leads to a set of improved and verified models for discontinuities caused by changes in waveguide dimensions, E-plane, H-plane, and angular displacements, corner rounding, burrs, and other errors. These models form the basis for our uncertainty analysis.

A more detailed examination shows that the error introduced by E-plane, H-plane, and angular displacements can be accurately modeled by a shunt susceptance (positive or negative) that is roughly a quadratic function of small mechanical displacements. As a result, standard first-order error propagation techniques fail to propagate these displacement errors. To circumvent this limitation, we develop a Monte Carlo approach capable of propagating displacement errors and their changing distributions and correlations with frequency through the entire calibration and measurement process.

We also show that displacement errors introduce a systematic bias in VNA calibrations that, unlike changes in aperture dimensions, cannot be eliminated by simple averaging. We demonstrate that multiline thru-reflect-line (TRL) calibrations [10]–[12] are particularly susceptible to the systematic bias introduced by these symmetric and roughly quadratic errors, and that this bias is not averaged out by the multiline algorithm.

Finally, we use our uncertainty analysis to assess the accuracy of thru-short-match (TSM) and thru-short-radiating-open [TS(RO)] calibrations [13], which do not suffer to the same extent from the bias introduced by mechanical displacements. Our uncertainty analysis also leads to an explicit procedure for objectively assessing the accuracy of the match and radiating open calibration standards, and choosing the best weighting scheme based on the quality of the test ports and match standards themselves.

II. Multiline TRL Calibration

We began our study of multiline TRL calibrations in this frequency range with the comparison of four state-of-the-art WM-380 (WR 1.5) [14] calibration sets we obtained from contractors working in the Defense Advanced Research Projects Agency's (DARPA) Terahertz Electronics Program. Each calibration kit had four roughly quarter-wavelength and four roughly eight-wavelength shims. These shims served as transmission-line standards.

Manuscript received November 24, 2010; accepted January 20, 2011. Date of publication April 05, 2011; date of current version October 28, 2011. This work was supported by the Defense Advanced Research Projects Agency's Terahertz Electronics Program.

The author is with the National Institute of Standards and Technology, Boulder, CO 80305 USA (e-mail: dylan@ boulder.nist.gov).

Color versions of one or more of the figures in this paper are available online at http://ieeexplore.ieee.org.

Digital Object Identifier 10.1109/TTHZ.2011.2127370

[1]NIST does not endorse commercial products. Product information is given only to more completely specify the experimental conditions. Other products may work as well or better.

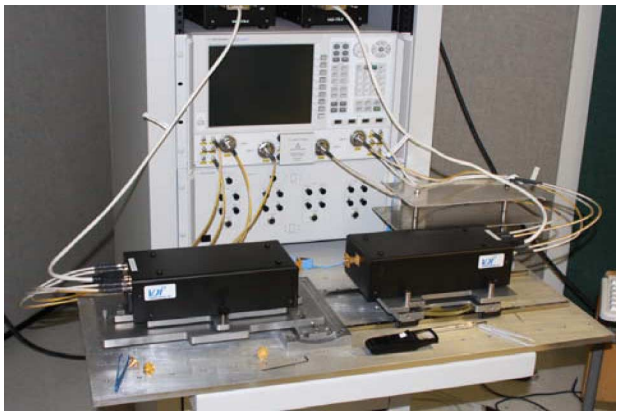

Fig. 1. The rail system we built to constrain the movement of the extension heads and cables.

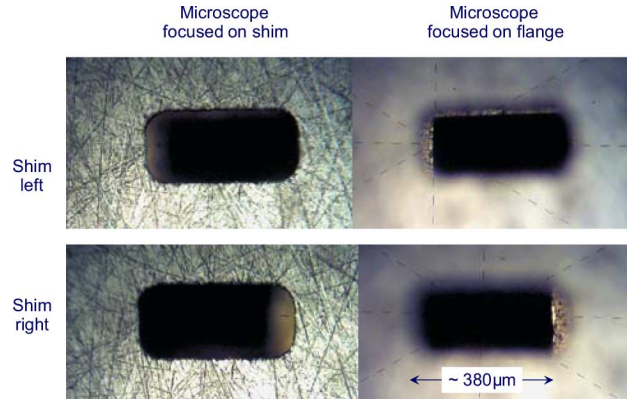

Fig. 2. Photographs of shims placed on top of the flanges on a test port. The microscope is focused on the surface of the shims in the photographs on the left, and on the flange below the shims in the photographs on the right. The shims have been pushed to the left in the top two photographs and to the right in the bottom two photographs.

A. Instrumentation Errors

We started with an overall assessment of the repeatability limits and instrumentation errors of our VNA, which consisted of an Agilent PNA-X and a pair of extension heads manufactured by Virginia Diodes, Inc. During all of the experiments we held the temperature at 23 °C±0.5 °C, with typical temperature deviations of about ±0.2 °C.

We had great difficulty making measurements without damaging the shims. We also found that once a shim was bent or warped, it not only degraded the quality of the calibrations, but became more likely to bind on the alignment pins in the future. We addressed this problem by constructing the rail system shown in Fig. 1 to constrain the motion of the heads.

The second most significant source of instrumentation error we identified was due to changes in the electrical length of the cables supplying the local oscillator signal to the two extension heads. We found that movement of the heads, even after the heads are moved back to their initial positions, led to differences in the forward and reverse transmission phases about their mean. We speculate that this phase change is due to the inevitable bending of the cables that the movement entails, resulted in changes of the electrical length of these cables that persist even after the heads are moved back to their initial position.

We found that our rail system helped reduce this source of measurement error, and added cable trays to the rail system to better support the cables and further constrain their movement to a single repeatable path. Finally, we performed repeated thru measurements during our experiments to track the phase drift in the local oscillator signals supplied to the heads. We then normalized the measured transmission phases to the nearest available thru measurement, typically taken within only 5 or 10 minutes of the transmission measurement. These steps allowed us to reduce our overall transmission phase drift during a typical experiment from about 20 degrees to only a few degrees.

B. Shim Repeatability and Consistency

The leftmost two photographs in Fig. 2 show a typical shim as seen through a microscope. The fabrication process necessitates the rounded corners. However, the dimensions were chosen by the manufacturer to provide a first-order match to the guide impedance.

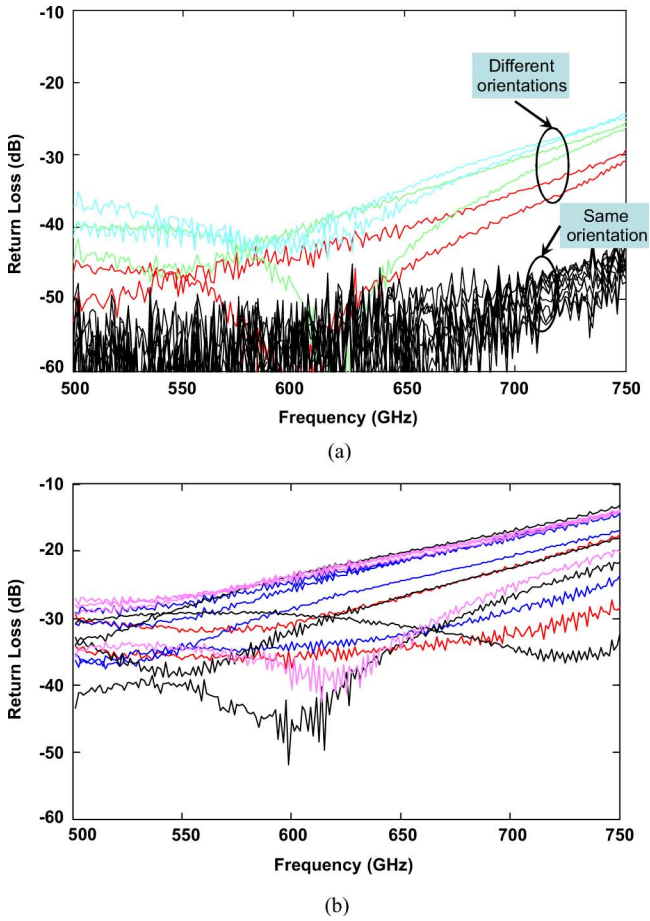

(a)

(b)

Fig. 3. Repeated measurements of the reflection coefficients of the shims (a) Single shim (b) Shims from different calibration sets.

Fig. 3 shows repeated measurements of the reflection coefficients of the shims as corrected by a TRL calibration based on one measurement of a single shim. Fig. 3(a) compares the repeated measurements of the reflection coefficient of the same

shim used in the TRL calibration, and shows repeatability levels for a single shim on the order of −50 dB[2].

The figure also shows repeated measurements performed after the shim was turned upside down, rotated 180 degrees, and both turned upside down and rotated 180 degrees. These measurements show that when the orientation of the shim on the test port is changed, that repeatability degrades to approximately −40 dB. This indicates that, while the test set is extremely repeatable, the shims themselves are not symmetric.

Fig. 3(b) compares measurements of different shims to each other, this time corrected by a TRL calibration employing a roughly quarter-wave and a roughly eighth-wave shim. This shows that the shims attain a consistency of about −30 dB at the low end and only −15 dB at the high end, illustrating the importance of their differences.

Appendix I summarizes a study of the dominant sources of uncertainty in rectangular-waveguide VNA calibrations, and presents closed form expressions for the errors. Out of all of the error mechanisms we studied in the appendix, only the electrical impact of an E-plane displacement increased as a function of frequency due to its capacitive behavior. The impact due to H-plane displacements, which are primarily inductive, and errors due to other mechanisms, dominate at the low end of the band, and either decreased or stayed constant with increasing frequency. This suggests that E-plane displacements are, in fact, a significant factor behind the differences between the measurements of the reflection coefficients of the shims. For this reason, we will now focus our attention on the impact of E-plane displacements in TRL calibrations as a way of better understanding what appears to be the dominant source of error in TRL calibrations. Later in the paper, when we turn our attention to other calibration types, we will consider all of the error mechanisms studied in Appendix I together.

C. Mechanical Alignment

Fig. 2 also illustrates the magnitude of the mechanical E-plane and H-plane displacements we observed as the shims sit on the test ports. We used photographs such as these and a micrometer on the microscope stage with a digital encoder to show that our shims moved an average of 37 μm on the test-ports flanges. Similar measurements showed that the test ports themselves moved an average of only 11.5 μm with respect to each other when mated. We note that the larger movement of the shims was intentionally introduced by the manufacturer to prevent the shims from binding on the flange's alignment pins during mounting and dismounting.

D. Systematic Bias in the TRL Calibration

Fig. 4, which is based on the closed-form expressions for waveguide discontinuities in given in Appendix I, shows the dependence of the normalized admittance at the interface between two sections of WM-380 (WR 1.5) rectangular waveguide as a function of the mechanical E-plane displacement between them.

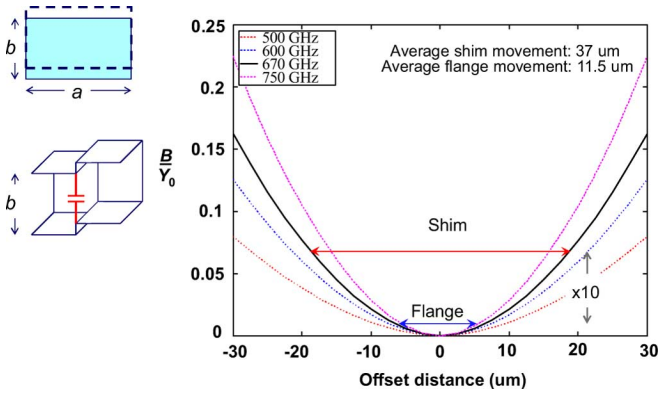

Fig. 4. Normalized admittance created by lateral displacement of two waveguide interfaces in a WM-380 (WR 1.5) calibration. The figure shows that the effect of the shim-to-flange displacements is approximately ten times larger than the effects of flange-to-flange displacements.

The admittance corresponds to a shunt capacitance at the junction, is a symmetric function of the mechanical displacement, and is a roughly quadratic function of the displacement when the displacement is small. This is because these displacements introduce the same positive capacitive discontinuity regardless of whether the step between two flanges is an upward or a downward step.

Since the excess capacitance due to E-plane displacements is always positive, statistical variations in the mechanical E-plane displacement will, in general, introduce a net positive bias in the excess capacitance at the interface between the waveguide flanges. Fig. 5 illustrates this with a histogram of the normalized admittance at 670 GHz generated by a Monte Carlo simulation. Here we assumed a maximum mechanical E-plane displacement of ± 18.5 μm, and plotted the histogram for two mechanical distributions, a rectangular distribution and an arc-sine distribution [15].[3] Despite the fact that the mechanical displacements are equally positive and negative, the figure clearly shows that the normalized admittance is always positive.

We have also labeled the mean values of the two distributions plotted in Fig. 5. We see clearly that, with increased averaging, the overall mean of the random admittance will approach a positive value near one half of the maximum possible admittance, introducing a systematic error in the calibration that cannot be reduced by simple averaging alone.

There is a similar negative effect due to H-plane and angular displacements. While H-plane and angular displacements do not usually have as large an impact on the calibration as E-plane displacements do, they are also roughly quadratic for small displacements. H-plane displacements result in a negative admittance at the interface, and tend to cancel E-plane displacements. This is particularly true at the lower end of the band, where the admittance due to E-plane displacements is smallest and the (negative) admittance due to H-plane displacements is largest. Nevertheless, the admittance due to E-plane displacements generally dominates that due to H-plane displacements, particularly

[2]We speculate that the repeatability of a single shim in the same orientation is so high because gravity may pull the shim into the same position each time it is measured despite the ability of the shim to move around the flange's alignment pins.

[3]A rectangular distribution corresponds to a freely moving displacement between two fixed limits or within a rectangle. An arc-sine distribution arises when the movement is constrained to a circle, as might arise for shims with circular holes whose mechanical movement is constrained by alignment pins.

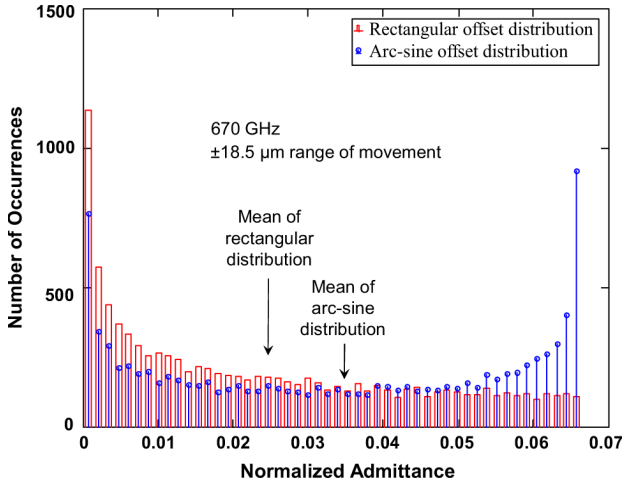

Fig. 5. Histogram of normalized admittance showing the admittance distribution due to a rectangular offset distribution with bars and an arc-sine distribution with circles.

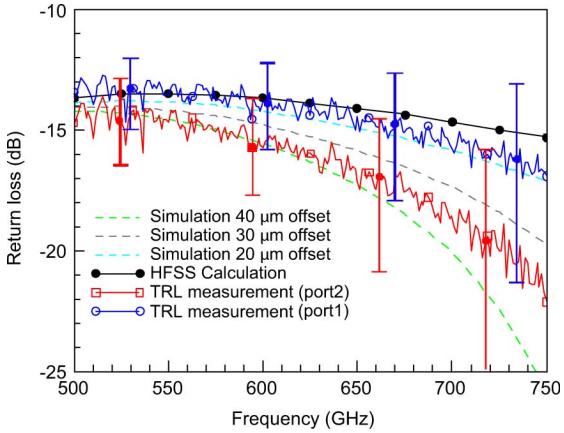

Fig. 6. TRL measurements of a radiating open and their standard uncertainties compared to HFSS calculations and simulations of calibrations based on standards displaced in the E-plane.

at the high end of the band. Thus we choose here to illustrate the importance of the quadratic nature of these errors with E-plane displacements.

The Monte Carlo uncertainty analysis we will discuss later includes E-plane, H-plane, and angular displacements, as well as the other error mechanisms discussed in Appendix I. Care was also taken in that analysis to include the correlations between E-plane and H-plane displacements. In particular, we accounted for the opposite signs of the susceptance caused by E-plane and H-plane displacements, and the natural cancellation that occurs when both are present, in that more rigorous and complete analysis.

Fig. 6 compares the refection coefficient of a radiating open-ended waveguide, as measured by a multiline TRL calibration based on eight shims, to HFSS simulations. The open-ended waveguide was embedded in a precision UG-387 flange (with pins) of the type described in [16].

The error bars in the figure represent standard uncertainties calculated from the orthogonal distance regression method, as implemented in [11], [12]. This method uses the overall lack of fit of the calibration data to the calibration model to estimate the uncertainty in the results. While this method generally captures any errors that manifest themselves as a lack of consistency between the measurements upon which the calibration is based, including errors due to E-plane and H-plane displacements, it is not capable of identifying systematic bias in the calibration. Nevertheless, the uncertainties predicted by the method are quite large and are consistent with the differences between the measurements and simulations.

To further investigate the source of the measurement error in our TRL calibrations, we also plotted simulations in Fig. 6 showing how a measurement of the radiating open would be perturbed by E-plane shim displacements[4] of 20 μm, 30 μm and 40 μm in our TRL calibration. These displacements are comparable to the actual E-plane displacements we measured under a microscope.

Not only is the bias in the measurements shown in Fig. 6 on both ports in the same direction, as we would expect from our previous arguments, but it is consistent with our predictions from the E-plane-displacement simulations. Thus Fig. 6 illustrates not only the high level of uncertainty we expect in our TRL calibrations due to E-plane displacements, but also the bias that we expect those displacements to introduce into our TRL calibrations.

We also examined measurements of radiating opens with the other TRL calibrations we performed, including the median calibration based on all of the 32 shims in the four calibration kits we had access to, and observed similar discrepancies. We attributed the fact that these discrepancies were not reduced by additional averaging in the multiline TRL calibrations to the bias introduced by displacements in the calibrations.

III. TSM Calibration

The principal reason that the TRL calibrations are sensitive to E-plane displacements is that the alignment holes in the shims must be made large enough to prevent them from binding on the flange's alignment pins as they are removed. However, rectangular-waveguide match standards do not have this constraint as they employ direct flange-to-flange connections with tighter tolerances. This suggests that TSM calibrations might be more accurate than TRL calibrations. Hence, we decided to study TSM calibrations, and to develop a full uncertainty analysis that includes all of the error mechanisms discussed in Appendix I.

A. Precision Waveguide Loads

We first found large ripples in TSM calibrations based on rectangular-waveguide loads intended for use as verification artifacts. These loads were fabricated at Virginia Diodes, Inc. by inserting a machined absorber directly in the waveguide channel, and a temporal analysis showed that the ripples in the calibrations were due to reflections off the machined absorber.

To circumvent this problem, Virginia Diodes, Inc. fabricated a pair of precision loads for us by inserting low-reflection-coefficient attenuators before the load element itself. The intent was to lower the reflections off the machined absorber. This strategy was extremely successful, and eliminated almost all of the ripple we observed in our early TSM calibrations.

[4]H-plane displacements were ignored in these simulations.

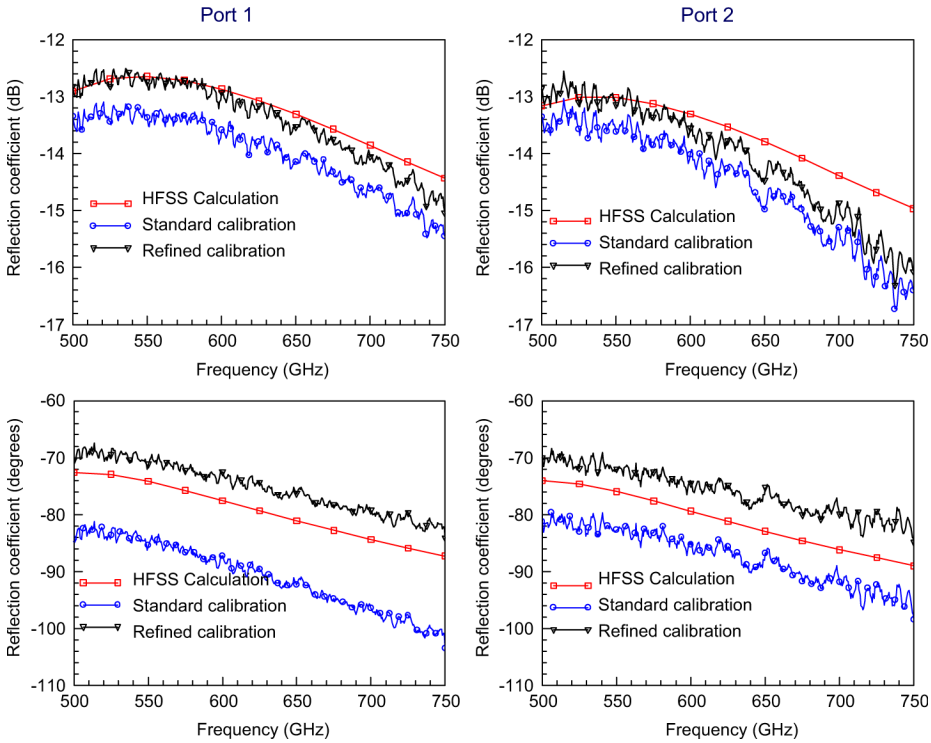

Fig. 7. Comparison of radiating opens corrected with a TSM calibration and numerical HFSS simulations. The HFSS simulations for the two ports differ slightly because of small differences in the aperture dimensions on the ports. The curves labeled "Standard calibration" used calibrations based on conventional standard definitions. The curves labeled "Refined calibration" employed the equivalent definitions of [17], which account for the reduced number of flange-to-flange connections when connecting thru and short standards with first-order corrections for imperfections in the connections.

Fig. 7 compares measurements of radiating opens, as corrected by TSM calibrations based on these precision loads, to HFSS calculations. The curves labeled "Standard calibration" correspond to measurements corrected by a straightforward TSM calibration based on standard definitions for the load, thru, and short. The curves labeled "Refined calibration" correspond to calibrations performed with the equivalent definitions of [17], and will be discussed in greater detail in the next section.

The improvement we achieve with our standard calibration over the results we obtained with the earlier TRL calibration is considerable (compare to Fig. 6), as expected from our previous analysis of the impact of E-plane displacements on calibration accuracy. Improvements over the TRL calibration were also seen in reflection-coefficient measurements of a long transmission line, corrected by the TSM calibration.

B. Correction Formalism

The use of TSM calibrations in rectangular waveguide introduces a new problem not present in TRL calibrations: the number and type of flange connections present during the measurement of the DUT are not preserved throughout the calibration process. In fact, when calibrating with a flat short, the shunt parasitic elements at the interface between the flange and the short are shorted out, and the thru connection is formed with only a single flange-to-flange connection, not two flange-to-flange connections, as is the case when measuring a DUT. Only the measurements of the calibration's match standards have the same number of flange-to-flange connections present as when the DUT is measured, and even here the interfaces may not be identical.

To address this, we based our "refined" calibrations on the "equivalent" standard definitions of [17], which we summarize in Appendix II. These definitions not only account for the reduced number of flange-to-flange connections when connecting to thru and short standards, but they allow us to make first-order corrections for imperfections in these connections.

In addition, the equivalent standard definitions of [17] allow the reference plane to be set in an ideal waveguide, or to be moved directly into a waveguide section containing the DUT. Setting the reference plane in the waveguide section containing the DUT, which is routine in on-wafer TRL calibrations, provides additional rigor in the calibration and correction process [17]. The curves labeled "Refined calibration" in Fig. 7 illustrate the improvement obtained with the equivalent definitions of [17]. In this refined calibration, the reference plane was placed at the end of the test ports where the actual radiation took place, rather than in an ideal perfectly centered test port.

C. Uncertainty Analysis

We developed a Monte Carlo uncertainty analysis,[5] based on the closed-form expressions described in Appendix I, to complement the correction formalism of [17]. The uncertainty analysis accounts for imperfect aperture dimensions, E-plane, H-plane, and angular displacements between guides, corner

[5]Estimating the uncertainties of TSM calibrations from orthogonal distance regression is difficult, as the TSM calibration is not as highly overdetermined as multiline TRL calibrations.

TABLE I
MEASURED WAVEGUIDE DIMENSIONS

Port	a			b			Wall uniformity	Corner rounding
	mean (μm)	σ (μm)	range (μm)	mean (μm)	σ (μm)	range (μm)	range (μm)	range (μm)
Test Port 1 (1 1-08m)	378.5	3	±3.75	176.2	3.4	±6	±5	<5
Test Port 2 (1 1-10m)	386.2	5.2	±7.75	185.5	3.4	±6.25	±5	<7
Line Port 1 (3 1-07m)	389	2.9	±4.5	201.4	2.1	±3	±2.5	<6
Line Port 2 (3 1-07u)	388.8	0.7	±1	197.1	2.0	±3	±2.5	<4
Precision Load (3 1-10)	381.6	1.1	±1.25	197	4.1	±5.5	±5	<5
Precision Load (3 1-20)	384.1	2.9	±3	199.1	2.1	±3.25	±5	<5

rounding, burrs on edges of the waveguide aperture, test-set drift and the other errors studied in the appendix. Unlike standard first-order linear uncertainty analyses and the orthogonal-distance-regression method employed in [11], [12], our Monte Carlo analysis was designed to handle uncertainties with a quadratic nature and the systematic bias they introduce into calibrations.

Table I summarizes the mechanical measurements we used to characterize the aperture dimensions of our rectangular waveguide test ports and the calibration and verification artifacts we used. The table reports both the standard deviations and the range of our repeated measurements. We also assessed the uniformity of the waveguide wall by setting the crosshairs of our microscope objective parallel to the wall, and then adjusting the stage in a direction perpendicular to the wall to measure the maximum and minimum deviations. This resulted in a worst-case deviation of the wall from a straight line. The dimensional data in Table I was used to include the impact of errors in both the height and width of the guides in our Monte Carlo simulations. These simulations also account for any cancellation of effects due to opposite signs of the susceptances at the waveguide interfaces.

We used rectangular distributions based on the maximum ranges for the measured mechanical parameters in Table I in our Monte Carlo analysis. These rectangular distributions avoided the occasionally large and unphysical deviations caused by Gaussian distributions in Monte Carlo analyses.

We also made molds of the interfaces by placing thin foils of silver solder between the flanges. Fig. 8 shows one of these molds. We used these molds to measure the displacements of the waveguide apertures. The means of these measurements are listed in Table II.

However, we found that the measured displacements could at times be as large as 25 μm. This was due to the combined effects of the lateral displacement of the aperture with respect to the alignment pins and holes in the flange, the average ± 6 μm lateral movement between the flanges, and to nonuniformity in the wall dimensions. From these displacement measurements we estimated that the displacements of the waveguide apertures from the means we measured could be as large as ± 10 μm, with the rest of the displacement being due to the roughly ± 6 μm lateral movement between the flanges. Thus we based our Monte Carlo analysis on the measured means in Table II with a ± 10 μm rectangular distribution and an additional displacement between the flanges with a ± 6 μm arc-sine distribution.[3] In implementing the arc-sine distribution, we correlated the

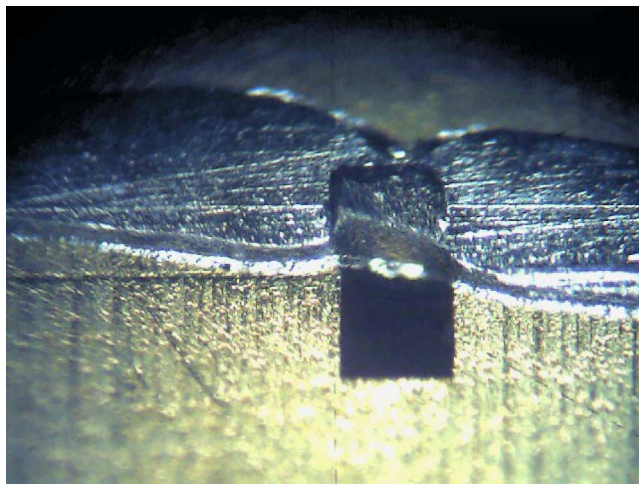

Fig. 8. Mold of the waveguide apertures formed in a thin foil of silver solder.

TABLE II
MEANS OF MEASURED DISPLACEMENTS BETWEEN FLANGES

Interface		H-plane (μm)	E-plane (μm)
TP1 (1 1-08m)	TP2 (1 1-10m)	15.5	8.33
TP1 (1 1-08m)	LineP1 (3 1-07m)	4	10
TP2 (1 1-10m)	LineP1 (3 1-07u)	11	1.5
TP1 (1 1-08m)	Load 1 (3 1-10)	1	8.125
TP2 (1 1-10m)	Load 1 (3 1-10)	3.75	4.8
TP1 (1 1-08m)	Load 2 (3 1-20)	9.25	1.06
TP2 (1 1-10m)	Load 2 (3 1-20)	3.17	5.71

E-plane and H-plane displacements to properly account for any possible addition or cancellation of the positive and negative admittances from these related mechanisms.

We also investigated the impact of corner rounding and angular misalignments, but concluded that they were small enough to be safely excluded from the analysis of these guides.

We included test-set drift in the analysis by performing TSM calibrations both before and after the DUT measurements. Then, we formed a combined calibration based on all of the measurements for use in correcting DUTs, but switched between the before and after calibrations when running the Monte Carlo simulations. This strategy allowed us to simulate the impact of the monotonic component of the test-set drift during the measurements, based on the actual drift measured during the experiment.

Finally, we used the results of the Monte Carlo analysis to form a covariance matrix that captures the uncertainty in the calibration. This allows a number of DUTs to be corrected after the

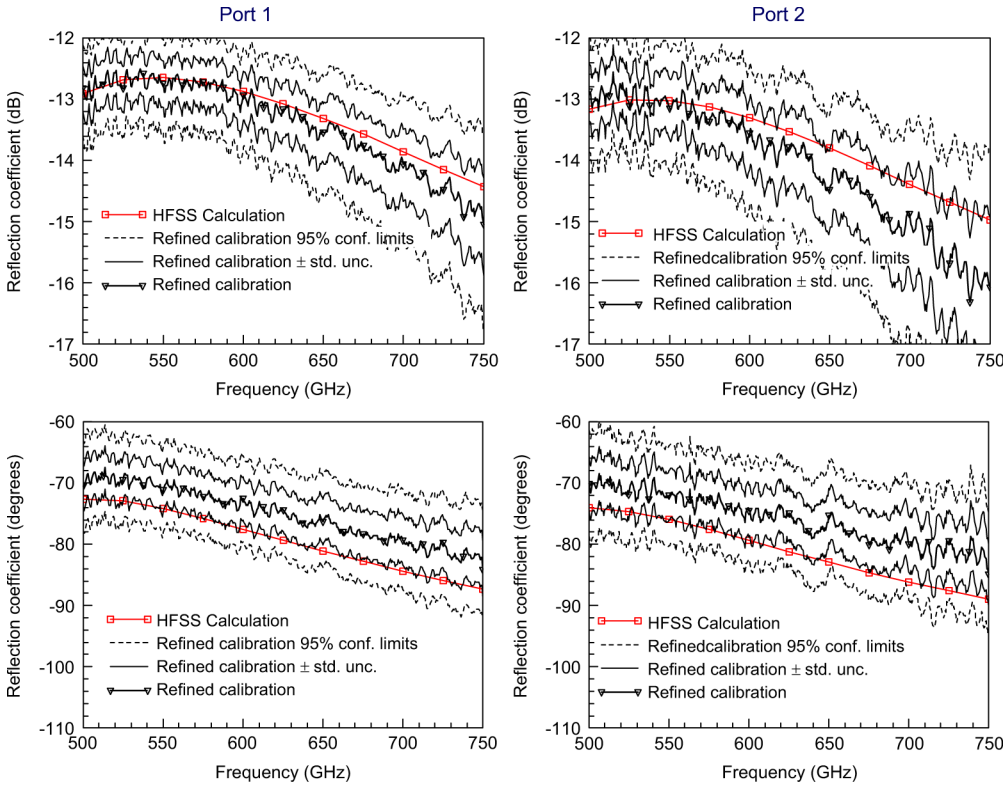

Fig. 9. Measurements of the reflection coefficients of radiated opens corrected with TSM calibrations and their uncertainties compared to HFSS simulations.

fact without requiring that the Monte Carlo analysis be rerun. Although this approach does not allow us to estimate the distributions of the DUT measurements, it does capture all of the uncertainties we identified in the calibration, including the mechanical displacements with a quadratic nature, and propagates them forward to the DUT measurements.

D. Verification

To verify our uncertainty analysis, we compared measurements of well-behaved artifacts to their estimated uncertainties. Fig. 9 compares measurements of radiating opens and the standard uncertainties estimated from the Monte Carlo analysis to HFSS simulations. The figure also illustrates our ability to propagate uncertainties to both the magnitude and phase of the reflection coefficient with the covariance matrices estimated by our Monte Carlo simulations. Not only are the uncertainties achieved with the TSM calibration shown in Fig. 9 much lower than the uncertainties achieved earlier with the multiline TRL calibration (see Fig. 6), but the deviations from the HFSS simulations are usually near or below the standard uncertainties of the measurements. In addition, the HFSS simulations are always within the 95% confidence limits of the measurements.

Fig. 10 compares measurements of a roughly 2.5 cm long section of rectangular waveguide with the uncertainties in those measurements. Fig. 10(a) compares the measured reflection coefficient to its standard uncertainty [18]. The low values of the measured reflection coefficients provide further evidence that the reference impedance of the TSM calibration has been set correctly. We also see that these reflection coefficients are both low and comparable to our estimates of their standard uncertainties, providing further evidence that we have arrived at reasonable estimates of the reference impedance of the calibration and its uncertainty.

Fig. 10(b) compares the measurements of the magnitudes of the forward and backward transmission coefficients of the long transmission line to the standard uncertainty of these measurements. The notch just above 550 GHz is due to a water line at this frequency. (We used the same scale factor for the left and right axes of this and other figures to facilitate a comparison of the measurements and their estimated uncertainties.)

While our analysis appears to have slightly underestimated the actual error in the measurement, our estimated uncertainties are again reasonably consistent with the level of unexplained measurement deviations.

Fig. 10(c) compares the measured phase of the long section of rectangular waveguide section to its uncertainty after we de-trended the phase by subtracting the theoretical phase estimated from the waveguide's length and cutoff frequency. The overall offset between the forward and backward phase measurements was likely due to drift in the electrical lengths of the cables. Again, the small unaccounted-for variations in the phase seem quite consistent with the estimated uncertainties plotted in the figure. Together, Fig. 10(b) and 10(c) provides good evidence that we have properly set the tracking terms in the VNA's calibration error model, and that our uncertainties in the tracking terms of the calibration are reasonably correct.

Fig. 11 shows measurements of an offset short constructed by terminating our long section of rectangular waveguide with a flat short. Again, we attribute the notch in the reflection coefficient

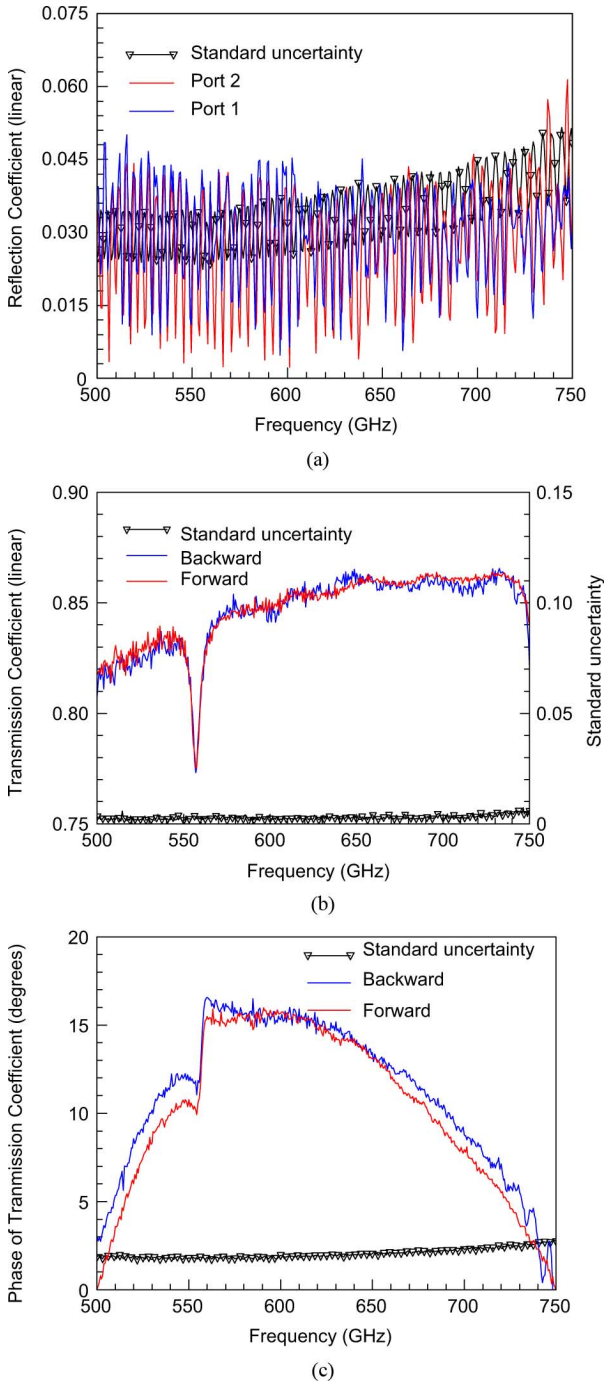

Fig. 10. Measurements of a 2.5 cm long transmission line corrected with a TSM calibration and their uncertainty estimates. (a) Magnitude of the reflection coefficient. (b) Magnitude of the transmission coefficient. (c) Detrended phase of the transmission coefficient.

just above 550 GHz to a water absorption line. Here also, the ripples and unexplained artifacts in the measurements are not only low, but consistent with the uncertainties calculated from our Monte Carlo analysis. This provides further evidence that we have properly set the tracking and effective test-port match in the VNA's error model, and that our uncertainties in those terms are reasonable.

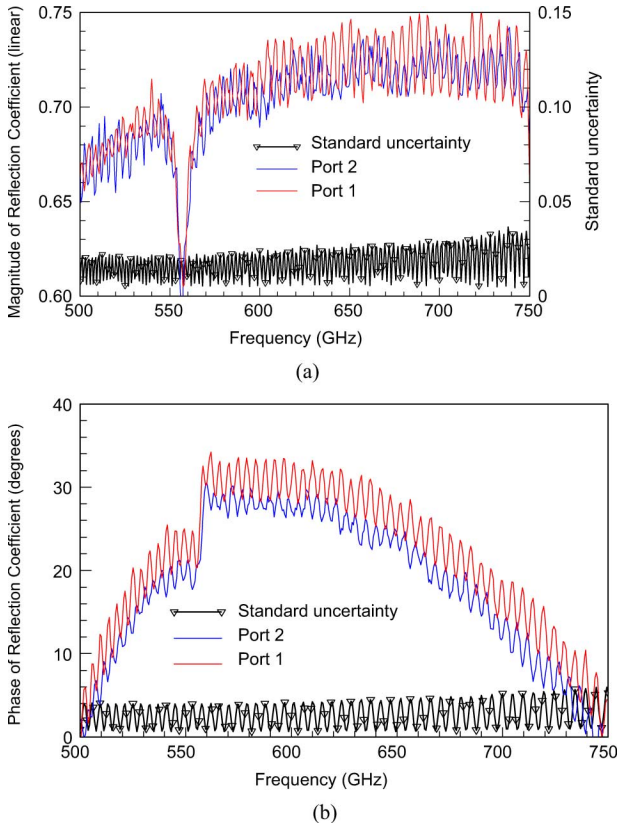

Fig. 11. Measurements of the reflection coefficient of an offset short corrected with a TSM calibration and their uncertainties. (a) Reflection-coefficient magnitude. (b) De-trended reflection-coefficient phase.

IV. Setting the Calibration Reference Impedance With Radiating Opens

Accurately setting the reference impedance is usually the most difficult aspect of VNA calibrations. Traditionally, radiating opens have been used as verification standards for checking the reference impedance of rectangular waveguide calibrations, and we have followed this approach thus far. However, in [13] Liu and Weikle argue that, because radiating open-ended rectangular waveguides do not suffer from flange misalignment, they may actually better set the reference impedance of rectangular-waveguide calibrations at millimeter-wave frequencies than do transmission lines and loads.

The accuracy with which the reference impedance can be set with radiating opens and precision loads depends on the quality of the test ports, the loads, and the number of loads available. We can use our Monte Carlo uncertainty analysis to evaluate these factors systematically and then objectively determine how to best set the reference impedance of rectangular-waveguide calibrations.

A. Assessment of Our Standard Test Ports

To illustrate the approach, we applied our uncertainty analysis to our calibration kit and standard test ports, which were of relatively low quality. We first took photographs of the apertures of our standard test ports and the precision loads fabricated at VDI under a microscope. While the burrs on the precision loads

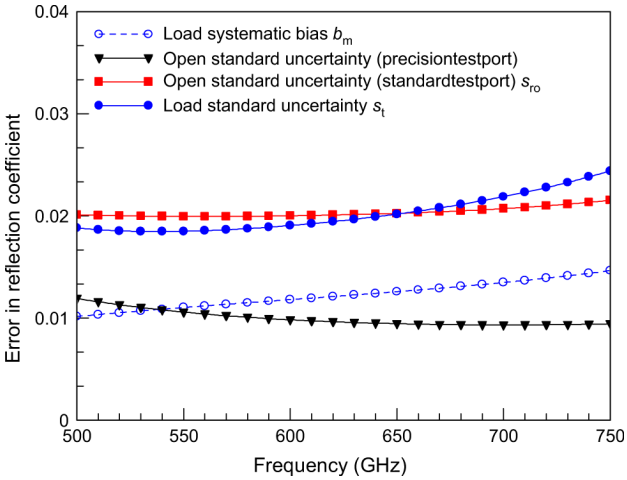

Fig. 12. Comparison of the estimated standard uncertainty and systematic bias of our precision loads, radiating opens on our standard test port and radiating opens on our precision test ports.

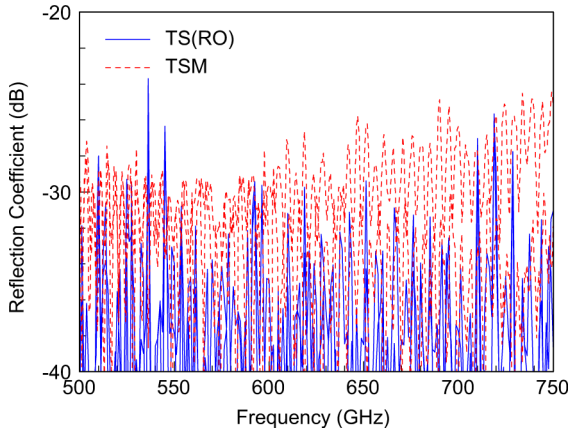

Fig. 13. Comparison of measurements of a long rectangular-waveguide section calibrated by TSM with standard test ports and TS(RO) with precision test ports.

were too small to measure under our microscope, the burrs on our standard test ports averaged 11 μm in size, and were relatively easy to see and quantify. We incorporated this information into our uncertainty model for the radiating open, and then used our Monte Carlo simulator to compare our uncertainty in the reflection coefficients of the radiating open and one of our precision loads.

Fig. 12 shows the results of the procedure. The solid line with squares shows the standard uncertainty of the reflection coefficient of the radiating open we calculated with our Monte Carlo simulator due to: 1) the uncertainty in the geometry of the aperture; 2) the uncertainty in the calculations of the impedance of the radiating open; 3) the uncertainty due to reflections off of the pins on the flange; and 4) the uncertainty due to the burrs at the test-port aperture.

We then compared the standard uncertainty of the reflection coefficient of the radiating test port to the standard uncertainty of the reflection coefficient of the precision load calculated with our Monte Carlo simulator. The latter uncertainty arose from our uncertainty in the geometry of the test-port and precision-load apertures and our uncertainty in transverse displacements between the test port and the loads. This uncertainty is shown by a solid line and with circles in Fig. 12.

The two standard uncertainties shown in Fig. 12 are comparable, an indication that the radiating open at the end of our standard test ports and the precision match will set the reference impedance of a calibration with similar accuracy. We confirmed this by comparing the reflection coefficients of a long section of rectangular waveguide measured with our TRM calibration and a TS(RO) calibration, and observed no significant differences in the results.

B. Precision Test Ports

We also investigated a second, better set of test ports with burrs of only 5 μm in size. The reduction in the size of the burrs from 11 μm to 5 μm is of great importance, not only because the uncertainty in the reflection coefficient in (8) of Appendix I is proportional to the square of the size of the burrs, but because these smaller burrs also allowed us to more accurately measure the width and height of the test ports. This improvement in our ability to set the reference impedance is shown in the curve with triangles of Fig. 12.

Fig. 13 illustrates the improvement obtained in the measurement of the reflection coefficients of a long section of rectangular waveguide when we used a TS(RO) calibration and our precision test ports compared to a TSM calibration with standard test ports. The occasional "spikes" in the curves corrected by the TS(RO) calibration shown in Fig. 13 are consistent with the sharp variations in the reflection coefficient of radiating opens due to reflections off the alignment pins we observed in the scaled experiments described in Appendix I.

C. Optimal Weighting of TSM(RO) Calibrations

The orthogonal distance regression algorithm [11], [12] allows us to assemble TSM(RO) calibrations that make use of both radiating opens and precision loads to optimally set the reference impedance of the calibration. The comparable standard uncertainties in Fig. 12 indicate that we should equally weight the radiating open standard and a precision load when we use our standard test ports to achieve an optimal result. Likewise, the figure indicates that we should apply a greater weight to the open when measured with our precision test ports.

While only one radiating open is available on each test port to assist in setting the reference impedance for each calibration, a number of match standards can be fabricated and tested for this purpose, allowing the overall uncertainty in the reference impedance to be reduced further by averaging. However, as Fig. 12 shows, systematic bias due to displacements, burrs, and other error mechanisms will limit the improvement in accuracy possible by averaging, and indicates that we should consider this systematic bias when determining how to weight the radiating open and match standards in TSM(RO) calibrations. We can determine optimal weighting coefficients that take this bias into account with the following procedure.

The random component of the variance s_r^2 of each match standard can be estimated from $s_r^2 = b_m^2 - s_t^2$, where b_m is the mean bias of a single match standard (curve labeled "Load systematic bias" in Fig. 12) and s_t is the total standard uncertainty of the match standard (curve labeled "Load standard uncertainty" in

Fig. 12). We can estimate an overall effective variance s_e^2 of the n available match standards from $s_e^2 = b_m^2 + (1/n)s_r^2$. Then, applying: 1) a weight of $1/s_{ro}^2$ to the radiating-open standard, where s_{ro} is its total standard uncertainty (curve labeled "Open standard uncertainty" in Fig. 12) and 2) a weight of $1/(ns_e^2)$ to each of the n match standards gives an optimal result.

Once the proper weights have been chosen and applied to the calibration algorithm, the calibration can be performed and the Monte Carlo algorithm can be used to estimate the uncertainties in the calibration as described earlier.

V. Software

We have encapsulated all of these analysis methods in a freeware package [19] that allows the user to quickly assess interface parameters with the models we developed, create the equivalent standard definitions described in [17], assess the level of bias introduced into the calibrations, and perform the Monte Carlo uncertainty analyses described in this paper.

VI. Conclusion

A detailed analysis of our multiline TRL calibrations at these frequencies led us to conclude that their measurement error is limited by systematic bias introduced primarily by E-plane and H-plane displacements, and that this error cannot be reduced by averaging. We then showed that TSM calibrations based on precision loads and TS(RO) calibrations based on radiating open-ended test ports reduce transverse displacements significantly, and provide attractive alternatives with greater accuracy.

We verified the accuracy of our TSM and TS(RO) calibrations by developing a full uncertainty analysis that captures all of the errors described in Appendix I. We not only showed that the uncertainty analysis provides reasonable estimates of the accuracy of these calibrations, but that it provides a systematic way of setting weights in optimal TSM(RO) calibrations based on both load and radiating open standards.

Our Monte Carlo simulator calculates systematic bias in the equivalent standard definitions we employed and allows the user to remove that bias from the results. However, we did not feel that our present dimensional measurements were accurate enough to investigate the efficacy of this approach at this time, and did not remove that systematic bias from any of the results presented here.

Appendix I
Closed–Form Expressions for Rectangular-Waveguide Interfaces

In this appendix, we compare analytic approximations given in [1], [5]–[9], [20] for waveguide discontinuities to each other and to simulations performed with HFSS. These analytic approximations form the basis of our uncertainty analysis, and are included in the freeware package [19] used to obtain the results we reported on in this paper.

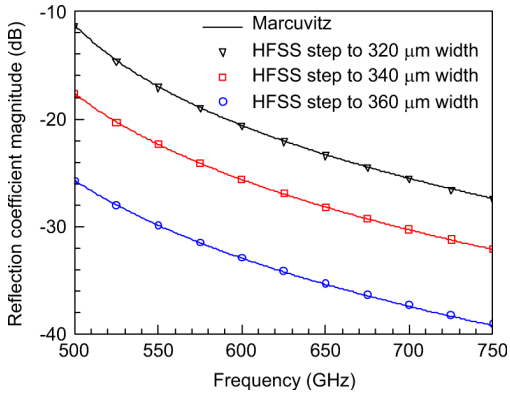

Fig. 14. Comparison of closed-form approximations given in Marcuvitz to a step in the width of a WM-380 (WR 1.5) rectangular waveguide. The nominal width of the guide is $380\ \mu$m.

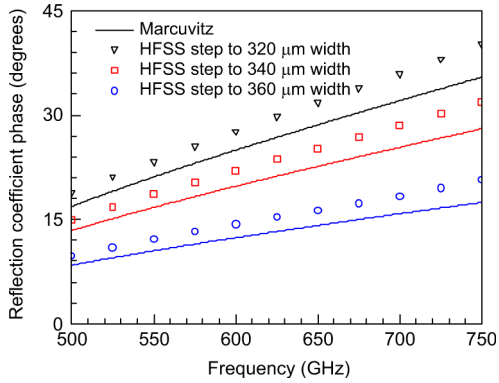

Fig. 15. The phase of the reflection coefficients shown in Fig. 13.

Step in Aperture Width a: Marcuvitz [6] gives closed-form approximations for impedance transformers and shunt admittances describing steps in the width or height in a section of rectangular waveguide. For example, Marcuvitz developed the approximations [6]

$$\frac{Z_2}{Z_1} \approx \frac{\lambda_{g2} a_2}{\lambda_{g1} a_1}\left(1+\beta+\frac{1}{2}\beta^2\right) \tag{1}$$

and

$$\frac{B}{Y_1} \approx -\frac{\lambda_{g1}}{2\,a_1}\beta^2\left(\frac{1+\beta}{1-\frac{1}{2}\beta}\right)\ln\left(\frac{2}{\beta}\right)\left(1-\frac{27}{8}\frac{Q+Q'}{1+8\ln\left(\frac{2}{\beta}\right)}\right) \tag{2}$$

for the normalized impedance change Z_2/Z_1 and admittance B/Y_1 at a discontinuity between a guide with width a_1 connected to a guide of width a_2, where $\beta = 1 - a_2/a_1$, $Q_i = 1 - \sqrt{1-(2a_i/3\lambda_0)^2}$, λ_0 is the free-space wavelength, and λ_g is the guided wavelength. Figs. 14 and 15 compare the closed form approximations for a small step in width of rectangular waveguide from (1) and (2) to the magnitude and phase of the reflection coefficient we calculated with HFSS. The figure shows that the approximations of (1) and (2) from [6] are remarkably accurate for these small steps in width.

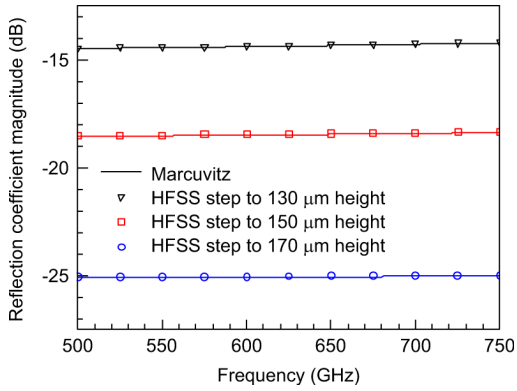

Fig. 16. Comparison of closed-form approximations given in Marcuvitz to a step in the height of a WM-380 (WR 1.5) rectangular waveguide. The nominal height of the guide is $190\ \mu$m.

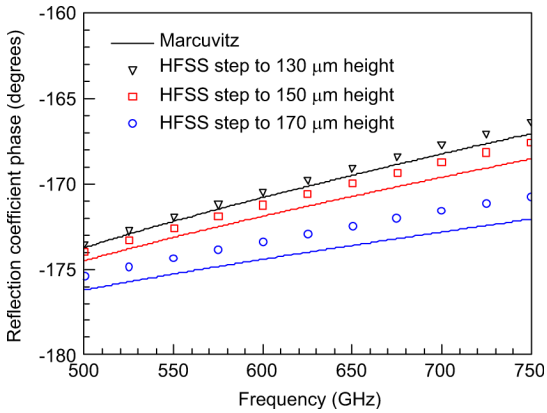

Fig. 17. Phase of the reflection coefficients shown in Fig. 16.

Step in Aperture Height b: Marcuvitz also developed the approximation [6]

$$\frac{B}{Y_0} \approx 2\frac{b_1}{\lambda_{g1}}\left(\frac{\delta}{2}\right)^2\left(\frac{2\ln\left(\frac{2}{\delta}\right)}{1-\delta}+\frac{17}{16}\left(\frac{b_1}{\lambda_{g1}}\right)^2\right) \tag{3}$$

for the normalized admittance B/Y_0 created by a step in height at a junction between two guides of differing height, where $\delta = 1 - b_2/b_1$ and the change of impedance at the junction is given by $Z_2/Z_1 \approx b_2/b_1$. Figs. 16 and 17 compare this approximation to our HFSS simulations, again showing remarkable agreement.

E-Plane and H-Plane Displacements: Marcuvitz [6], Hunter [5], and Bannister *et al.* [1] proposed approximations based on impedance transformers and shunt admittances to model H-plane displacements (displacements in the width direction), and Marcuvitz and Hunter proposed approximations for E-plane displacements (height direction). Hunter fit the reflection coefficient Γ created by a displacement at the interface with

$$\Gamma \approx 10^{\left(\left(\sum_k u_k(\chi-\alpha)^k\right)\log_{10}\tau+\left(\sum_k v_k(\chi-\alpha)^k\right)\right)} \tag{4}$$

where, for an E-plane displacement, the fitting parameters were $\div = b_1/\lambda_{g1}$, $\alpha = 0.3$, $\tau = \Delta b/b_1$, $u_0 = 1.833$, $u_1 = 0.276$, $u_2 = 0.73$, $v_0 = 0.293$, $v_1 = 2.133$, $v_2 = 0.78$ and $v_3 = 19.69$. For an H-plane displacement, the fitting parameters were $\chi = a_1/\lambda_0$, $\alpha = 0.7$, $\tau = \Delta a/a_1$, $u_0 = 1.75$, $u_1 = -0.332$, $u_2 = -2.71$, $u_3 = -3.57$, $v_0 = 0.635$, $v_1 = -1.562$, $v_2 = 0.44$ and $v_3 = -7.63$. Hunter even went so far as to suggest that accurately displaced rectangular waveguide sections might be useful as calibration standards.

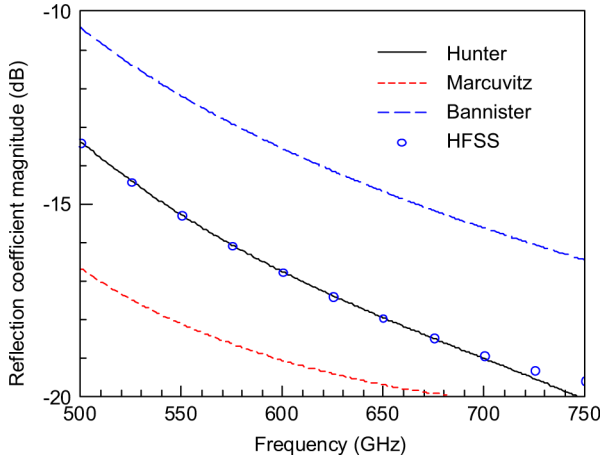

Fig. 18. Comparison of closed-form approximations for an H-plane displacement of $60\ \mu$m in a WM-380 (WR 1.5) rectangular waveguide.

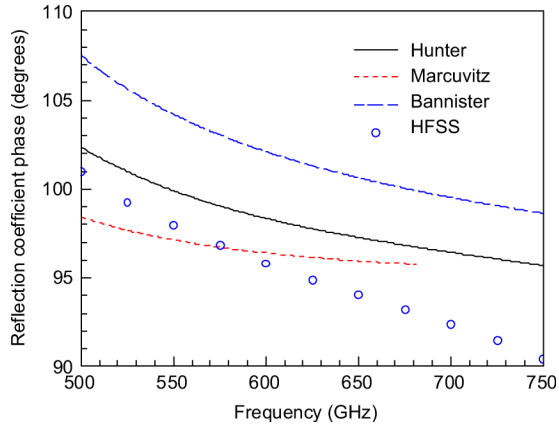

Fig. 19. Phase of the reflection coefficients shown in Fig. 18.

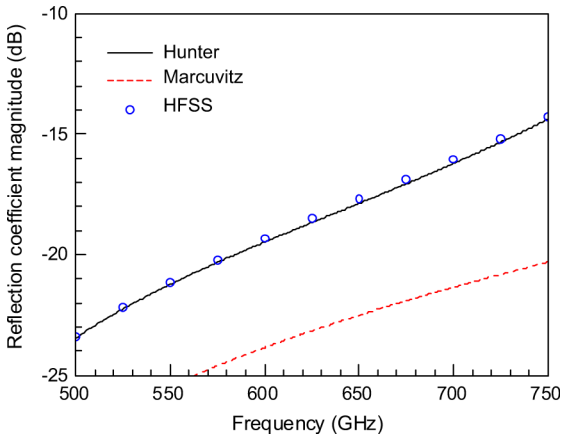

Fig. 20. Comparison of closed-form approximations for an E-plane displacement of $40\ \mu$m in a WM-380 (WR 1.5) rectangular waveguide.

Figs. 18–21 show typical comparisons of these approximations and HFSS simulations. Based on these comparisons, we concluded that the expressions proposed by Hunter in [5]

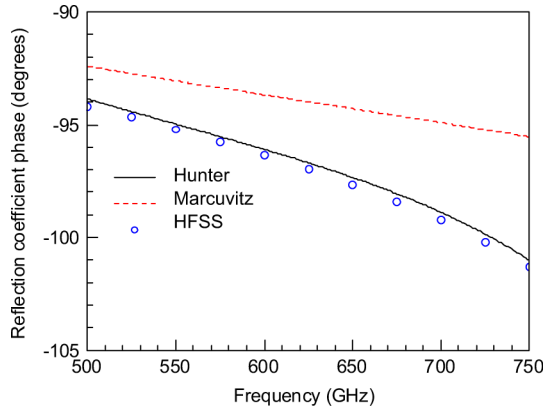

Fig. 21. Phase of the reflection coefficients shown in Fig. 20.

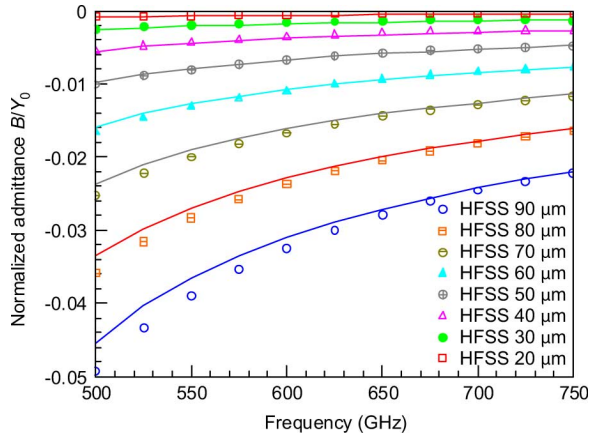

Fig. 22. Comparison of closed-form approximations for the normalized admittance at an interface between two WM-380 (WR 1.5) rectangular waveguides with and without rounded corners.

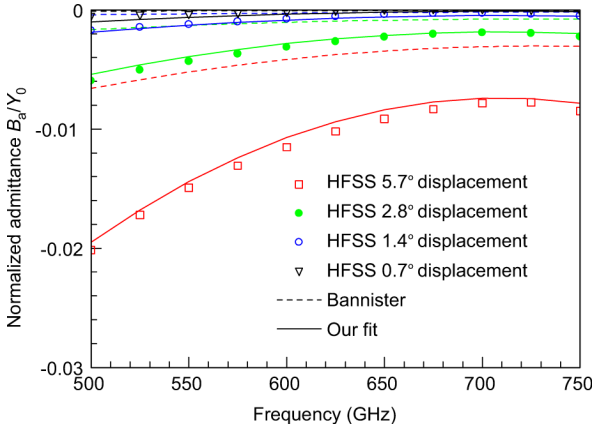

Fig. 23. Comparison of the approximation from Bannister and our approximation to HFSS calculations for the normalized admittance at an interface as a function of the angular alignment between two WM-380 (WR 1.5) rectangular waveguides.

were superior to the expressions proposed by Marcuvitz and Bannister.

Corner Rounding: Cohn showed that the cutoff frequency of waveguides with complicated end shapes but with parallel top and bottom walls can be approximated well with the cutoff frequency of a rectangular waveguide of the same height and a cross section of equal area [21]. In 1961, Cohn pointed out in [22] that the significance of this had been lost in the "technical graveyard," and explicitly discussed the application to rounded corners in rectangular waveguides. Brady later studied this in greater detail in [9], and Anson, *et al.* applied this approach to approximating the impedance of rectangular waveguide with rounded corners in [8].

However, these approximations did not include the shunt admittance that arises at the interface between rectangular waveguide with and without rounded corners. We used HFSS simulations to calculate this admittance and developed the approximation

$$\frac{B_{\mathrm{r}}}{Y_0} \approx -0.305 \frac{\lambda_{\mathrm{g}}}{a} \left(\frac{r_{\mathrm{corner}}^2}{a\,b} \right)^{1.3} \tag{5}$$

for the normalized admittance B_{r}/Y_0 at the interface, where λ_{g} is the guided wavelength in the unperturbed rectangular waveguide, r_{corner} is the radius of curvature of the rounded corners, and a and b are the width and height of the guide. Fig. 22 compares our HFSS results to the approximate fit (5). Our software package uses (5) to approximate the shunt admittance and [8] to approximate the impedance change at the interface.

Angular Displacement: We also compared the approximations for the admittance caused by angular displacements at the interface between two rectangular waveguides suggested by Bannister, *et al.* in [1] to HFSS simulations. The results in Fig. 23 show significant differences. We found that the fit

$$\frac{B_{\mathrm{a}}}{Y_0} \approx -\left(0.000225\,\theta^2 + \left[0.01 + 0.0049\,\theta^2 \right] \left| \frac{a}{\lambda_0} - 0.9 \right|^2 \right) \tag{6}$$

shown in Fig. 23, where θ is the angular displacement in degrees between the two guides, provided a better fit than the approximation suggested by Bannister, *et al.* in [1].

Reflection Coefficient of a Radiating Open: We used a series of Legendre polynomials to fit the reflection coefficient of radiating open-ended waveguides calculated with the method of [23]. We then compared our fit to HFSS calculations and the hybrid method of [24], as described in [25]. The differences in reflection coefficients were less than 0.005. Thus, we assigned an uncertainty with a rectangular distribution of ± 0.005 to the real and imaginary parts of our fit to results from the method of [23], and included this in our uncertainty analysis.

Reflections From Alignment Pins and Other Flange Components: We assessed the impact of reflections from the alignment pins of a UG 387 flange experimentally on the reflection coefficient of a radiating open with scaled WR 90 experiments over the frequency range of 8.2–12.4 GHz, as discussed in [25]. We then fit the results to the radar cross section of a cylinder, and added in a term to account for large reflections observed when the pin was in the near field of the aperture. This resulted in the rough approximation

$$\Delta\Gamma_{\mathrm{pin}} \sim 0.018 \sqrt{\frac{h_{\mathrm{pin}}\, r_{\mathrm{pin}}}{R^2} \frac{h_{\mathrm{pin}}}{\lambda_0} \left(\left(\frac{\lambda_0}{R} \right)^2 + 60 \left(\frac{\lambda_0}{R} \right)^5 \right)} \tag{7}$$

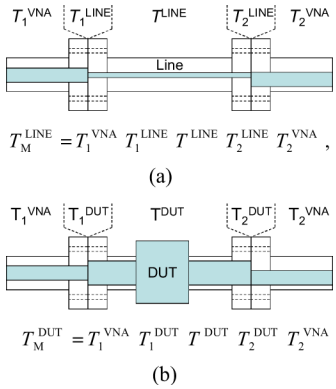

Fig. 24. The line standard during calibration and the device under test during measurement. The method of [17] is based on forcing the two equations in this figure to be consistent. (After [17].) (a) Calibration (b) Measurement.

for the average impact $\Delta\Gamma_{\rm pin}$ on the reflection coefficient of the radiating open, where $h_{\rm pin}$ is the height of the alignment pin, $r_{\rm pin}$ is its radius, R is the distance between the center of the aperture and the pin, and λ_0 is the free-space wavelength.

We also built an HFSS model for the UG 387 flanges we used. The model included the pins, the holes for the screws, the boss specified in [16], and the edge of the flange.

We were unable to run the HFSS simulations in the far field of the aperture because the problem size became too large for our computers. However, we were able to run the simulations for WM-2540 (WR 10), WM-1650 (WR 6) and WM-710 (WR 4) openings in the flange, and simulated reflections approximately 3 times larger than the reflections off of the pins.

Thus we multiplied (7) by a factor of 6 before incorporating it into our error analysis. The first factor of two accounted for the fact that we had two pins on each flange, and the factor of 3 accounted for the best estimate we had available for the additional impact of the boss and edge of the flange on the reflection coefficient of our radiating opens.

Burrs: We used HFSS to develop the rough approximation

$$\Delta\Gamma \approx -10\,i\left[\left(\frac{h_{\rm burr}}{a}\right)^2 + 2000\left(\frac{h_{\rm burr}}{a}\right)^6\right]\cos\left(\frac{4\pi}{3}\frac{y}{a}\right) \tag{8}$$

for the reflection coefficient $\Delta\Gamma$ of a burr of height, width, and depth $h_{\rm burr}$ located on the broad wall of the aperture and displaced from the center of the guide by a distance y. We also developed the rough approximation [25]

$$\Delta\Gamma_{\rm open} \approx -6\left[\left(\frac{h_{\rm burr}}{a}\right)^2 + 1000\left(\frac{h_{\rm burr}}{a}\right)^6\right] \times\left[\cos\left(\pi\frac{y}{a}\right) + 2i\,\cos\left(\frac{4\pi}{3}\frac{y}{a}\right)\right] \tag{9}$$

for the change $\Delta\Gamma_{\rm open}$ in the refection coefficient of a radiating open due to the same burr on the broad wall of a radiating aperture. Our simulations indicated that burrs on the narrow wall of the aperture had a much smaller impact on reflections, and we neglected these burrs in our analysis.

Appendix II
Correction Algorithm

The calibration approach we used is described in [17]. It treats each flange interface as a whole, calculating the scattering parameters of each interface from the offsets and perturbations of both flanges. This enables it to account for the quadratic nature of the E-plane, H-plane, and angular displacements, since the positive and negative susceptances these introduce at an interface depend roughly on the square of the total displacement between the flanges and cannot be determined for one flange at a time.

The equivalent standard definitions of [17] were based on the fact that the DUT correction can be applied to calibration standards as well, and the result must yield the equivalent standard definition [17]. Referring to Fig. 24, we can show that the equivalent definition $T_{\rm DEF}^{\rm LINE}$ of a transmission-line standard used in the calibration is given by [17]

$$T_{\rm DEF}^{\rm LINE} \equiv \left[T_1^{\rm DUT}\right]^{-1} T_1^{\rm LINE}\, T^{\rm LINE}\, T_2^{\rm LINE}\left[T_2^{\rm DUT}\right]^{-1}, \tag{10}$$

where $T_1^{\rm LINE}$ and $T_2^{\rm LINE}$ are the cascade parameters describing the interface between the test ports and the line, $T_1^{\rm DUT}$ and $T_2^{\rm DUT}$ correspond to the discontinuity at the interface between the test ports and the device under test, and $T^{\rm LINE}$ is the cascade matrix of the line itself. For convenience, the impedance transformation between the line in the test port and the calibration standard are included in $T_1^{\rm LINE}$ and $T_2^{\rm LINE}$, rather than including them in $T^{\rm LINE}$.

The equivalent definition $T_{\rm DEF}^{\rm THRU}$ of a flush thru calibration standard is given by [17]

$$T_{\rm DEF}^{\rm THRU} \equiv \left[T_1^{\rm DUT}\right]^{-1} T^{\rm THRU}\left[T_2^{\rm DUT}\right]^{-1} \tag{11}$$

where $T^{\rm THRU}$ are the cascade parameters describing the interface between the two test ports. Note that the equivalent definition of even a simple flush thru no longer corresponds to a perfect connection (identity matrix) between two lines. The equivalent definition (11) takes into account not only any discontinuities at the interface between the test ports themselves, but also any discontinuities between the imperfect test ports and the interface to the device under test.

The equivalent definition $T_{\rm DEF}^{\rm SHORT}$ of a flat short is given by [17]

$$T_{\rm DEF}^{\rm SHORT} \equiv \left[T_1^{\rm DUT}\right]^{-1} T^{\rm SHORT}\left[T_2^{\rm DUT}\right]^{-1}. \tag{12}$$

(See Appendix I of [17] for a discussion of how cascading can be performed when the calibration elements do not have any transmission.) Since most discontinuities in rectangular waveguide can be described as shunt admittances or impedance transforms, $T^{\rm SHORT}$ corresponds to the scattering parameters of a perfect short. However, this would not be the case if, for example, the test port had discontinuities that could be modeled as a series inductance.

Like the flush short, radiating opens do not have their own interface dimensions. Rather, their definitions are completely dependent on the geometry and properties of the test port. Thus (12) applies to radiating open standards as well, with $T^{\rm SHORT}$ replaced by $T^{\rm RO}$, the reflection coefficient of the radiating open

at the test-port interface as defined in the test-port access line, and $T_{\rm DEF}^{\rm SHORT}$ replaced by $T_{\rm DEF}^{\rm RO}$, the equivalent definition of the radiating open.

Finally, the equivalent definitions $T_{\rm DEF}^{\rm MATCH}$ of a match and $T_{\rm DEF}^{\rm OSHORT}$ of an offset short are given by [17]

$$T_{\rm DEF}^{\rm MATCH} \equiv \left[T_1^{\rm DUT}\right]^{-1} T_1^{\rm OFF} T^{\rm OFF} T^{\rm MATCH} T^{\rm OFF} T_2^{\rm OFF} \times \left[T_2^{\rm DUT}\right]^{-1} \quad (13)$$

$$T_{\rm DEF}^{\rm OSHORT} \equiv \left[T_1^{\rm DUT}\right]^{-1} T_1^{\rm OFF\_S} T^{\rm OFF\_S} T^{\rm SHORT} T^{\rm OFF\_S} \times T_2^{\rm OFF\_S} \left[T_2^{\rm DUT}\right]^{-1}. \quad (14)$$

Here $T^{\rm OFF}$ and $T^{\rm OFF_S}$ represent the offset transmission line between the interface and the match or short; $T^{\rm MATCH}$ represents the reflection coefficient of the absorber itself.

ACKNOWLEDGMENT

First and foremost, the author thanks Dr. J. Hesler of Virginia Diodes, Inc., for providing many of the calibration artifacts used in this work, including the precision loads, and for numerous discussions of calibration and measurement issues at these frequencies. He also thanks A. Arsenovic of the University of Virginia for assisting in the measurements and for useful discussions, and A. Kerr of the National Radio Astronomy Observatory for an exceptionally careful reading of the manuscript and his insightful comments and recommendations. He also thanks B. Alpert of the National Institute of Standards and Technology for help fitting our HFSS measurements of radiating opens to Legendre polynomials; Drs. Ghasr and Zoughi at the Missouri University of Science and Technology for calculations of the reflection coefficient of radiating opens; and the staff at Teledyne Scientific, the Jet Propulsion Laboratory, and the University of Virginia for allowing him to test their calibration kits. Finally, the author thanks D. Gallagher at National Institute of Standards and Technology for the innovative design and construction of his rail system.

This work is a publication of the National Institute of Standards and Technology, an agency of the U.S. government, and is not subject to U.S. copyright. The views, opinions, and/or findings contained in this article/presentation are those of the author/presenter and should not be interpreted as representing the official views or policies, either expressed or implied, of either the Defense Advanced Research Projects Agency or the Department of Defense.

REFERENCES

[1] D. Bannister, E. J. Griffin, and T. E. Hodgetts, National Physical Lab., "On the dimensional tolerances of rectangular waveguide for reflectrometry at millimetric wavelengths," 1989.

[2] A. R. Kerr, E. Wollack, and N. Horner, "Waveguide flanges for ALMA instrumentation," ALMA Memo. 278, Nov. 1999 [Online]. Available: http://www.alma.nrao.edu/memos/

[3] A. R. Kerr, "Mismatch caused by waveguide tolerances,corner radii, and flange misalignment," Electronics Div. Tech. Note 215, Jan. 2010 [Online]. Available: http://www.gb.nrao.edu/electronics/edtn/edtn215.pdf

[4] "Guidelines on the evaluation of vector network analysers (VNA)," EURAMET/cg-12/v.01, 2007.

[5] J. D. Hunter, "The displaced rectangular waveguide junction and its use as an adjustable reference reflection," *IEEE Trans. Microw. Theory Techn.*, vol. 32, no. 4, pp. 387–394, Apr. 1984.

[6] N. Marcuvitz, *Waveguide Handbook*. New York: McGraw-Hill, 1951.

[7] R. E. Collin, *Foundations for Microwave Engineering*. New York: McGraw-Hill,, 1966.

[8] W. J. Anson, R. W. Beatty, D. M. Kerns, and W. T. Randy, "Investigations of the reflection from a junction of an ideal rectangular waveguide with one having rounded inside corners," in *PGMTT Nat.Symp. Dig.*, 1962, vol. 62, pp. 27–31.

[9] M. M. Brady, "Cutoff wavelengths and frequencies of standard rectangular waveguides," *Electron. Lett.*, pp. 410–412, 1969.

[10] R. B. Marks, "A multi-line method of network analyzer calibration," *IEEE Trans. Microw. Theory Techn.*, vol. 39, no. 7, pp. 1205–1215, Jul. 1991.

[11] D. F. Williams, C. M. Wang, and U. Arz, "An optimal vector-network-analyzer calibration algorithm," *IEEE Trans. Microw. Theory Techn.*, vol. 51, no. 12, pp. 2391–2401, Dec. 2003.

[12] D. F. Williams, C. M. Wang, and U. Arz, "An optimal multiline TRL calibration algorithm," in *IEEE MTT-S Int. Microw. Symp. Dig.*, Jun. 2003, vol. 3, pp. 1819–1822.

[13] Z. Liu and R. M. Weikle, "A reflectometer calibration method resistant to waveguide flange misalignment," *IEEE Trans. Microw. Theory Techn.*, vol. 54, no. 6, pp. 2447–2452, Jun. 2006.

[14] N. M. Ridler, R. A. Ginley, J. L. Hesler, A. R. Kerr, R. D. Pollard, and D. F. Williams, "Towards standardized waveguide sizes and interfaces for submillimeter wavelengths," in *21 Int. Symp. Space Terahertz Technol.*, Mar. 2010.

[15] *BIPM, IEC, IFCC, ISO, IUPAC, IUPAP, and OIML, Evaluation of Measurement Data-Supplement 1 to the 'Guide to the Expression of Uncertinay in Measurement'-Propagation of Distributions Using a Monte Carlo Method*, Vol. JCGM 101:2008, Int. Org. for Standardization, 2008.

[16] J. L. Hesler, A. R. Kerr, W. Grammer, and E. Wollack, in *18th Int. Symp. Space Terahertz Technology*, Mar. 2007.

[17] D. F. Williams, "Rectangular-waveguide vector-network-analyzer calibrations with imperfect test ports," in *Automatic RF Techniques Group Conf. Dig.*, Dec. 2010.

[18] *Guide to the Expression of Uncertainty in Measurement, International Organization for Standardization*, pp. 1-101, BIPM, IEC, IFCC, ISO, IUPAC, IUPAP, and OIML, 1993.

[19] D. F. Williams, Rectangular-waveguide calculator Nat. Inst. Standards and Technology (NIST), 2010 [Online]. Available: http://www.boulder.nist.gov/dylan

[20] D. Hill, "Reflection coefficient of a waveguide with slightly uneven walls," *IEEE Trans. Microw. Theory Tech.*, vol. 37, no. 1, pp. 244–252, 1989.

[21] S. B. Cohn, "Microw. coupling by large apertures," *Proc. IRE*, vol. 40, no. 6, pp. 696–699, Jun. 1952.

[22] S. B. Cohn, "Bones from the technical graveyard," *Microw. J.*, pp. 15–17, Nov. 1961.

[23] M. T. Ghasr, D. Simms, and R. Zoughi, "Multimodal solution for a waveguide radiating into multilayered structures-dielectric property and thickness evaluation," *IEEE Trans. Instrum. Meas.*, vol. 58, no. 5, pp. 1505–1513, May 2009.

[24] B. Zheng and Z. Shen, "Analysis of dielectric-loaded waveguide slot antennas by the hybrid mode-matching/moment method," *IEICE Trans. Commun.*, vol. E88-B, no. 8, pp. 3416–3427, Aug. 2005.

[25] D. F. Williams, M. T. Ghasr, B. Alpert, Z. Shen, A. Arsenovic, and R. M. Weikle, "Reflection Coefficient of radiating rectangular-waveguide test ports," *IEEE Microw. Wireless Compon. Lett.*, 2011, submitted for publication.

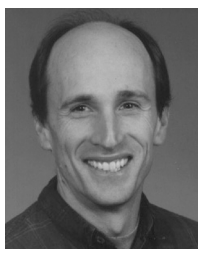

Dylan F. Williams (M'80–SM'90-F'02) received the Ph.D. degree in electrical engineering from the University of California, Berkeley, in 1986.

He joined the Electromagnetic Fields Division of the National Institute of Standards and Technology in 1989 where he develops metrology for the characterization of monolithic microwave integrated circuits and electronic interconnects. He has published over 80 technical papers.

Dr. Williams is the recipient of the Department of Commerce Bronze and Silver Medals, two Electrical Engineering Laboratory's Outstanding Paper Awards, two Automatic RF Techniques Group (ARFTG) Best Paper Awards, the ARFTG Automated Measurements Technology Award, and the IEEE Morris E. Leeds Award. He has also served a four-year term as Editor-in-Chief of the IEEE TRANSACTIONS ON MICROWAVE THEORY AND TECHNIQUES.